

# Analysis of adiabatic shear bands in heat-conducting elastothermoviscoplastic materials by the meshless local Bubnov–Galerkin method

R. C. Batra<sup>1</sup> and D. Spinello<sup>2,\*</sup>,<sup>†</sup>

<sup>1</sup>*Department of Engineering Science and Mechanics, Virginia Polytechnic Institute and State University, Blacksburg, VA 24061, U.S.A.*

<sup>2</sup>*The Bradley Department of Electrical and Computer Engineering, Virginia Polytechnic Institute and State University, Blacksburg, VA 24061, U.S.A.*

## SUMMARY

Transient finite coupled thermomechanical simple shearing deformations of a block made of an elastothermoviscoplastic material that exhibits strain and strain-rate hardening, and thermal softening are studied by using the meshless local Bubnov–Galerkin method. A local nonlinear weak formulation and a semidiscrete formulation of the problem are derived. The prescribed velocity at the top and the bottom surfaces of the block is enforced by using a set of Lagrange multipliers. A homogeneous solution of the problem is perturbed by superimposing on it a temperature bump at the center of the block, and the resulting nonlinear initial-boundary-value problem is solved numerically. We have developed an integration scheme to numerically integrate the set of coupled nonlinear ordinary differential equations.

The inhomogeneous deformations of the block are found to concentrate in a narrow region of intense plastic deformation usually called a shear band. For a material exhibiting enhanced thermal softening, it is shown that as the shear stress within the region of localization collapses, an unloading elastic shear wave emanates outward from the edges of the shear band. In the absence of an analytical solution, the computed results have been compared with those obtained by the finite element and the modified smoothed particle hydrodynamics methods. Copyright © 2008 John Wiley & Sons, Ltd.

Received 21 June 2007; Revised 10 February 2008; Accepted 7 April 2008

KEY WORDS: shear strain localization; meshless method; coupled thermomechanical deformations

## 1. INTRODUCTION

The term adiabatic shear is related to a localization phenomenon that occurs during high strain-rate plastic deformations such as machining, explosive forming, shock impact loading, ballistic

---

\*Correspondence to: D. Spinello, The Bradley Department of Electrical and Computer Engineering, Virginia Polytechnic Institute and State University, Blacksburg, VA 24061, U.S.A.

<sup>†</sup>E-mail: dspinell@vt.edu

penetration, fragmentation, ore crushing, impact tooling failure, and metal shaping and forming processes. The shear strain localization problems in metals (see e.g. [1]) are generally characterized by the formation of a narrow region of intense plastic deformation called an adiabatic shear band (ASB). Although heat conduction plays a significant role in determining the shear band width, it is called adiabatic since there is not enough time for the heat to be conducted away from the shear band. The shear strain localization has been observed in many materials such as steel, nonferrous metals, and polymers. The study of the phenomenon is important because progressive shearing within an ASB provides an undesirable mode of material resistance to imposed deformations; moreover, the bands are often precursors of ductile fracture in many metals deformed at high strain rates.

Recently, considerable research in computational mechanics has been devoted to the development of meshless methods. An objective of a meshless method is to eliminate or at least alleviate the difficulty of meshing the domain. Meshless methods may also alleviate some other problems associated with the finite element method (FEM), such as locking and element distortion. In many applications, they also provide smooth and accurate approximate solutions with a reduced number of nodes.

During the last two decades, several meshless methods for seeking approximate solutions of partial differential equations have been proposed. These include the element-free Galerkin [2], hp-clouds [3], the reproducing kernel particle [4], the diffuse element [5], the partition of unity finite element [6], the natural element [7], meshless Galerkin using radial basis functions (RBFs) [8], the meshless local Petrov–Galerkin (MLPG) [9, 10], the smoothed particles hydrodynamics (SPH) [11], the modified smoothed particle hydrodynamics (MSPH) [12], the meshless local boundary integral equation [13], the collocation method using RBFs [14], and the symmetric smoothed particle hydrodynamics (SSPH) [15]. All of these methods, except for the last six, use either shadow elements or a background mesh for evaluating integrals in the governing weak formulation of a problem.

The MLPG method has been successfully applied to several problems in mechanics: static linear plane elasticity [9]; vibrations of elastic planar bodies [16]; static analysis of beams [17]; static and dynamic analyses of functionally graded materials [18–21]; transient heat conduction in a bimaterial body [22]; wave propagation in bars with material interfaces [23] and in cracked beams [24]; static analysis of nonlinear electromechanical problems [25]; and the determination of stress concentration factors under static and dynamic loadings [26, 27]. To our knowledge it has not been applied to analyze a transient thermoviscoelastoplastic problem involving the localization of deformations into a narrow band.

The MLPG method is based on a local weak formulation of the governing equations and employs meshless interpolations for both the trial and the test functions. Bases for the trial functions are usually constructed with the moving least-squares (MLS) approximation [28]. In the Petrov–Galerkin formulation, the test functions may be chosen from a different space than the space of trial functions. Thus several variations of the method may be obtained (see e.g. [9] for discussion). The key ingredients of the MLPG method may be summarized as local weak formulation, MLS interpolation, Petrov–Galerkin projection, numerical evaluation of domain integrals, and computation of desired quantities at critical points.

Here we analyze simple shearing deformations of a block made of an elastothermoviscoplastic material with the MLPG6 method, i.e. the local Bubnov–Galerkin formulation, and we show that it captures well the localization of deformation and the emanation of an elastic unloading wave from the shear-banded region. In the constitutive relation for the material, strain and strain-rate

hardening, and thermal softening are considered. The problem is studied by introducing a local nonlinear augmented weak form (LNAWF) of coupled nonlinear governing equations with the nonhomogeneous essential boundary conditions. The prescribed velocities on the top and the bottom surfaces of the block are enforced by a set of Lagrange multipliers. From the LNAWF, a semidiscrete formulation is derived, and the constraint related to the nonhomogeneous essential boundary conditions is treated by introducing a transformation matrix that eliminates the constrained degrees of freedom. Since nodal variables do not equal values of unknowns at the nodes, standard time integration packages such as LSODE [29] cannot be employed. Therefore, the resulting reduced system of coupled nonlinear ordinary differential equations is integrated in time by a one-step algorithm, which can be regarded as both the first-order Adams–Moulton method and the first-order backward difference method [30]. The convergence at each time step is reached by Newton’s iterations. Good agreement between the computed results and the ones obtained with the FEM in [31] and with the MSPH method in [32] is achieved. For materials exhibiting enhanced thermal softening, it has been found that the shear stress drops very rapidly in the localization region, and an elastic unloading shear wave emanates outward from it. The numerically computed wave speed matches well with the analytical one, and the width of the region of localization is close to that observed experimentally [33] and to that obtained by the FE and the MSPH methods.

The remainder of the paper is organized as follows. In Section 2 we formulate the initial-boundary-value problem to be studied by presenting the governing equations, and initial and boundary conditions. In Section 3 we present the MLPG formulation of the initial-boundary-value problem by briefly outlining the MLS approximation, introducing the LNAWF, and obtaining from it the nonlinear semidiscrete formulation. In Section 4 we discuss the time integration scheme and compare the numerical solution with those obtained by the FE and the MSPH methods. Expressions for functions appearing in the domain integrals are reported in Appendix A.

## 2. FORMULATION OF THE PROBLEM

We analyze simple shearing deformations of a block made of an elastothermoviscoplastic material that lies between the planes  $y = \pm H$  as depicted in Figure 1. Only the  $x$ -component of velocity is taken to be nonzero. Equations governing deformations of the body are [1, 31]

$$\rho \dot{v}(y, t) = s'(y, t) \quad (1a)$$

$$\rho \dot{e}(y, t) = -q'(y, t) + s(y, t)v'(y, t) \quad (1b)$$

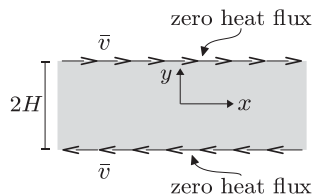


Figure 1. Geometry and kinematic boundary conditions of the problem.

$$\dot{\gamma}(y, t) = v'(y, t) \quad (1c)$$

$$\dot{\gamma}(y, t) = \dot{\gamma}_e(y, t) + \dot{\gamma}_p(y, t) \quad (1d)$$

$$q(y, t) = -\kappa \vartheta'(y, t) \quad (1e)$$

$$\dot{s}(y, t) = \mu \dot{\gamma}_e(y, t) \quad (1f)$$

$$\varrho \dot{e}(y, t) = \varrho c \dot{\vartheta}(y, t) + s(y, t) \dot{\gamma}_e(y, t) \quad (1g)$$

$$\dot{\gamma}_p(y, t) = \Lambda(y, t) s(y, t) \quad (1h)$$

$$k(y, t) \dot{\psi}(y, t) = s(y, t) \dot{\gamma}_p(y, t), \quad k(y, t) = k_0 \left( 1 + \frac{\psi(y, t)}{\psi_0} \right)^n \quad (1i)$$

$$\Lambda = \max \left\{ 0, \frac{1}{bs} \left( \left( \frac{s}{k_0(1-a\vartheta)(1+\psi/\psi_0)^n} \right)^{1/m} - 1 \right) \right\} \quad (1j)$$

Here, a superimposed dot indicates the material derivative with respect to time  $t$ , and the prime means derivative with respect to the space variable  $y$ . Furthermore,  $v$  is the  $x$ -component of velocity,  $s$  the shear stress,  $q$  the heat flux,  $\gamma$  the shear strain,  $\gamma_e$  and  $\gamma_p$  the elastic and the plastic parts of the shear strain, respectively,  $e$  is the specific internal energy,  $\vartheta$  the temperature rise,  $\psi$  an internal variable,  $\varrho$  the mass density,  $\kappa$  the thermal conductivity,  $c$  the specific heat, and  $\mu$  the shear modulus. The parameter  $k$  describes the work hardening of the material,  $a$  is the thermal softening parameter,  $b$  and  $m$  are the strain-rate hardening parameters,  $\psi_0$  and  $n$  are the work hardening parameters, and  $k_0$  is the yield stress in a quasi-static isothermal simple shear test. The plastic multiplier  $\Lambda$  is zero when the deformation is elastic and is positive for plastic deformations, see [1].

Equation (1a) is the balance of linear momentum, Equation (1b) the balance of internal energy, Equation (1c) the definition of the shear strain rate, and Equation (1d) the additive decomposition of the total shear strain rate into elastic and plastic parts. Equation (1e) is Fourier's law of heat conduction, Equations (1f) and (1g) are constitutive relations, and Equation (1h) is the flow rule with the plastic multiplier  $\Lambda$  given by Equation (1j). Equation (1i) describes the work hardening of the material due to plastic deformations. The yield surface is assumed to be given by

$$s = k_0(1-a\vartheta) \left( 1 + \frac{\psi}{\psi_0} \right)^n (1+b\dot{\gamma}_p)^m \quad (2)$$

whose radius increases due to strain and strain-rate hardening and decreases due to thermal softening.

We introduce the following nondimensional variables:

$$\begin{aligned}
 y &= H\bar{y}, & \gamma &= \bar{\gamma}, & \psi &= \bar{\psi}, & v &= H\dot{\gamma}_0\bar{v}, & t &= \frac{\bar{t}}{\dot{\gamma}_0} \\
 s &= k_0\bar{s}, & k &= k_0\bar{k}, & \Lambda &= \frac{\dot{\gamma}_0}{k_0}\bar{\Lambda}, & b &= \frac{\bar{b}}{\dot{\gamma}_0}, & \mu &= k_0\bar{\mu} \\
 \vartheta &= \frac{k_0}{\varrho c}\bar{\vartheta}, & \varrho &= \frac{k_0}{H^2\dot{\gamma}_0^2}\bar{\varrho}, & \kappa &= \varrho c H^2\dot{\gamma}_0\bar{\kappa}, & a &= \frac{\varrho c}{k_0}\bar{a}
 \end{aligned} \tag{3}$$

where quantities with an overbar are nondimensional, and  $\dot{\gamma}_0$  is the average shear strain rate. Substituting Equations (3) into Equations (1) and dropping the overbars from nondimensional variables, we get the following set of governing equations in nondimensional variables:

$$\varrho\dot{v} = s' \tag{4a}$$

$$\dot{\vartheta} = \kappa\vartheta'' + \Lambda s^2 \tag{4b}$$

$$\dot{s} = \mu(v' - \Lambda s) \tag{4c}$$

$$\dot{\psi} = \frac{\Lambda s^2}{(1 + \psi/\psi_0)^n} \tag{4d}$$

$$\Lambda = \max \left\{ 0, \frac{1}{bs} \left( \left( \frac{s}{(1-a\vartheta)(1+\psi/\psi_0)^n} \right)^{1/m} - 1 \right) \right\} \tag{4e}$$

Following [31], we assume that a homogeneous solution of Equations (4) under boundary conditions

$$v(-1, t) = -1, \quad v(1, t) = 1 \tag{5a}$$

$$\vartheta'(\pm 1, t) = 0 \tag{5b}$$

and initial conditions

$$v(y, 0) = y, \quad \vartheta(y, 0) = s(y, 0) = \psi(y, 0) = 0 \tag{6}$$

is perturbed when  $\psi = 0.1$ ,  $\vartheta = 0.1003$ , and  $\gamma = 0.0692$ . We seek a solution to the resulting initial-boundary-value problem with boundary conditions (5) and initial conditions

$$v(y, 0) = y \tag{7a}$$

$$\vartheta(y, 0) = 0.1003 + 0.1(1 - y^2)^9 \exp(-5y^2) \tag{7b}$$

$$s(y, 0) = \left( 1 + \frac{0.1}{\psi_0} \right)^n (1 - a\vartheta(y, 0))(1 + b)^m \tag{7c}$$

$$\psi(y, 0) = 0.1 \tag{7d}$$

The second term on the right-hand side of Equation (7b) represents a perturbation; its amplitude is chosen large enough to reduce the computational time required for deformations to localize at

$y=0$ . The peak in the shear stress–shear strain curve occurs at  $\gamma=0.093$ . Boundary condition (5b) implies that the surfaces  $y = \pm 1$  are thermally insulated. Thus all of the heat generated due to plastic dissipation is used to raise the temperature of the body. The inhomogeneous initial conditions imply that the temperature rise within the body is nonuniform.

Because of boundary conditions (5) and initial conditions (7), we assume that the solution exhibits the following symmetries/antisymmetries:

$$v(-y, t) = -v(y, t) \tag{8a}$$

$$\vartheta(-y, t) = \vartheta(y, t) \tag{8b}$$

$$s(-y, t) = s(y, t) \tag{8c}$$

$$\psi(-y, t) = \psi(y, t) \tag{8d}$$

Therefore, we solve the problem in the domain  $(0, 1)$  with initial conditions (7) and the following boundary conditions

$$v(0, t) = 0, \quad v(1, t) = 1 \tag{9a}$$

$$\vartheta'(0, t) = 0, \quad \vartheta'(1, t) = 0 \tag{9b}$$

### 3. MLPG FORMULATION

#### 3.1. Local nonlinear augmented weak form

Let  $\Omega_S^i \subseteq [0, 1]$ ,  $i = 1, 2, \dots, N$ , be a family of subdomains of the global domain  $[0, 1]$  such that  $\bigcup_{i=1}^N \Omega_S^i = [0, 1]$  and  $\Omega_S^i$  contains the  $i$ th node; note that  $\Omega_S^i$  need not be disjoint in the MLPG formulation. We introduce the following LNAWF of the problem on the  $i$ th subdomain  $\Omega_S^i$ . The equation

$$\begin{aligned} 0 = & \int_{\Omega_S^i} \tilde{v}_i \dot{v} \, dy - \int_{\Omega_S^i} \varrho^{-1} \tilde{v}_i s' \, dy + [\delta_0(\lambda_0 \tilde{v}_i + \tilde{\lambda}_0 v)]|_{\Gamma_S^{i-}} - [\delta_1(\lambda_1 \tilde{v}_i + \tilde{\lambda}_1(v-1))]|_{\Gamma_S^{i+}} \\ & + \int_{\Omega_S^i} \tilde{\vartheta}_i \dot{\vartheta} \, dy + \int_{\Omega_S^i} \kappa \tilde{\vartheta}_i' \vartheta' \, dy - \int_{\Omega_S^i} \tilde{\vartheta}_i \Lambda s^2 \, dy + [(1-\delta_0)\tilde{\vartheta}_i \vartheta']|_{\Gamma_S^{i-}} - [(1-\delta_1)\tilde{\vartheta}_i \vartheta']|_{\Gamma_S^{i+}} \\ & + \int_{\Omega_S^i} \tilde{s}_i \dot{s} \, dy - \int_{\Omega_S^i} \mu \tilde{s}_i (v' - \Lambda s) \, dy + \int_{\Omega_S^i} \tilde{\psi}_i \dot{\psi} \, dy - \int_{\Omega_S^i} \tilde{\psi}_i \Lambda s^2 \left(1 + \frac{\psi}{\psi_0}\right)^{-n} \, dy \end{aligned} \tag{10}$$

with  $\Lambda$  given by Equation (4e) must hold for all choices of test functions  $\tilde{v}_i$ ,  $\tilde{\vartheta}_i$ ,  $\tilde{s}_i$ ,  $\tilde{\psi}_i$ ,  $\tilde{\lambda}_0$ , and  $\tilde{\lambda}_1$ . Here,  $\tilde{v}_i \in L^2(0, 1)$ ,  $\tilde{\vartheta}_i \in H^1(0, 1)$ ,  $\tilde{s}_i \in L^2(0, 1)$ ,  $\tilde{\psi}_i \in L^2(0, 1)$ , and  $\tilde{\lambda}_0, \tilde{\lambda}_1 \in \mathbb{R}$ .

$$\delta_\zeta(\zeta) := \begin{cases} 1, & \zeta = \zeta \\ 0, & \zeta \neq \zeta \end{cases} \tag{11}$$

is the characteristic function, and  $\Gamma_S^{i-}$ ,  $\Gamma_S^{i+}$  are the left and the right boundary points of the subdomain  $\Omega_S^i$ . Since the MLS basis functions do not possess the Kronecker delta property, essential

boundary conditions (9a) cannot be imposed directly at the boundary nodes. Therefore, Lagrange multipliers  $\lambda_0$  and  $\lambda_1$  have been introduced. We emphasize that the homogeneous natural boundary conditions (9b) have been incorporated in the LNAWF. The variational statement expressed by Equation (10) can be derived by following classical arguments, see e.g. [34].

Since Equation (10) is required to hold for all choices of  $\tilde{v}_i, \tilde{s}_i, \tilde{\vartheta}_i, \tilde{\psi}_i, \tilde{\lambda}_0$ , and  $\tilde{\lambda}_1$ , Equations (4a), (4c), and (4d) and essential boundary conditions (9a) immediately follow from it. An integration by parts of the term involving  $\vartheta'$  and then exploiting the arbitrariness of  $\tilde{\vartheta}_i$  yields Equation (4b) and natural boundary conditions (9b).

### 3.2. Semidiscrete formulation

In order to seek an approximate solution of the nonlinear initial-boundary-value problem defined by Equation (10), we approximate fields  $v, \vartheta, s$ , and  $\psi$  by using the MLS basis functions [28]:

$$v^h(y, t) = \boldsymbol{\varphi}(y)^T \hat{\mathbf{v}}(t) \quad (12a)$$

$$\vartheta^h(y, t) = \boldsymbol{\varphi}(y)^T \hat{\boldsymbol{\vartheta}}(t) \quad (12b)$$

$$s^h(y, t) = \boldsymbol{\varphi}(y)^T \hat{\mathbf{s}}(t) \quad (12c)$$

$$\psi^h(y, t) = \boldsymbol{\varphi}(y)^T \hat{\boldsymbol{\psi}}(t) \quad (12d)$$

Here,  $\boldsymbol{\varphi}$  are basis functions, and  $\hat{\mathbf{v}}$  the vector of fictitious nodal velocities. For convenience, we collect the fictitious nodal unknowns and the Lagrange multipliers into the  $4N$ - and two-dimensional vectors:

$$\hat{\mathbf{u}}(t) := [\hat{\mathbf{v}}(t) \ \hat{\boldsymbol{\vartheta}}(t) \ \hat{\mathbf{s}}(t) \ \hat{\boldsymbol{\psi}}(t)]^T \quad (13a)$$

$$\boldsymbol{\lambda}(t) := [\lambda_0(t) \ \lambda_1(t)]^T \quad (13b)$$

where  $N$  is the number of nodes in the global domain  $[0, 1]$ .

In order to obtain  $4N + 2$  equations for the  $4N + 2$  unknowns  $\hat{\mathbf{u}}(t)$  and  $\boldsymbol{\lambda}(t)$ , we consider  $4N + 2$  independent test functions in Equation (10):

$$\tilde{v}_1, \dots, \tilde{v}_N, \quad \tilde{\vartheta}_1, \dots, \tilde{\vartheta}_N, \quad \tilde{s}_1, \dots, \tilde{s}_N, \quad \tilde{\psi}_1, \dots, \tilde{\psi}_N, \quad \tilde{\lambda}_0, \tilde{\lambda}_1 \quad (14)$$

We choose the support of the MLS basis function for the  $i$ th node to be the  $i$ th subdomain  $\Omega_S^i$ , and the related test function to be the MLS basis function. Therefore, since the test and the trial functions are chosen from the same space, we get the following local nonlinear Bubnov–Galerkin (MLPG6) semidiscrete formulation:

$$\mathbf{M} \dot{\hat{\mathbf{u}}}(t) = \mathbf{G}(\hat{\mathbf{u}}(t)) + \mathbf{L}^T \boldsymbol{\lambda}(t) \quad (15)$$

$$\mathbf{L} \hat{\mathbf{u}}(t) = \bar{\mathbf{u}} \quad (16)$$

where  $\mathbf{M}$  is a  $(4N \times 4N)$ -matrix, given by

$$\mathbf{M} = \text{DIAG}[\mathbf{D}, \mathbf{D}, \mathbf{D}, \mathbf{D}], \quad [\mathbf{D}]_{ij} = \int_{\Omega_S^i} \varphi_i \varphi_j \, dy, \quad i, j = 1, \dots, N \quad (17)$$

and  $\mathbf{L}$  is a  $(2 \times 4N)$ -matrix given by

$$[\mathbf{L}]_{1j} = [\delta_0 \varphi_j]_{\Gamma_S^{j-}}, \quad [\mathbf{L}]_{2j} = [-\delta_1 \varphi_j]_{\Gamma_S^{j+}}, \quad j = 1, \dots, 4N \quad (18)$$

Equation (16) is the affine constraint, with the 2-vector  $\bar{\mathbf{u}}$  given by

$$\bar{\mathbf{u}} = [0 \ 1]^T \quad (19)$$

The nonlinear operator  $\mathbf{G}$  appearing on the right-hand side of Equation (15) can be conveniently expressed as

$$\mathbf{G}(\hat{\mathbf{u}}(t)) = [\mathbf{G}^1(\hat{\mathbf{u}}(t)) \ \mathbf{G}^2(\hat{\mathbf{u}}(t)) \ \mathbf{G}^3(\hat{\mathbf{u}}(t)) \ \mathbf{G}^4(\hat{\mathbf{u}}(t))]^T \quad (20)$$

with

$$[\mathbf{G}^1(\hat{\mathbf{u}})]_i = \int_{\Omega_S^i} \varrho^{-1} \varphi_i \boldsymbol{\varphi}^T \hat{\mathbf{s}} \, dy \quad (21a)$$

$$[\mathbf{G}^2(\hat{\mathbf{u}})]_i = - \int_{\Omega_S^i} \kappa \varphi_i' \boldsymbol{\varphi}^T \hat{\boldsymbol{\vartheta}} \, dy + \int_{\Omega_S^i} \varphi_i \Lambda^h(\hat{\mathbf{u}}) (\boldsymbol{\varphi}^T \hat{\mathbf{s}})^2 \, dy \quad (21b)$$

$$[\mathbf{G}^3(\hat{\mathbf{u}})]_i = \int_{\Omega_S^i} \mu \varphi_i (\boldsymbol{\varphi}^T \hat{\mathbf{v}} - \Lambda^h(\hat{\mathbf{u}}) \boldsymbol{\varphi}^T \hat{\mathbf{s}}) \, dy \quad (21c)$$

$$[\mathbf{G}^4(\hat{\mathbf{u}})]_i = \int_{\Omega_S^i} \varphi_i \Lambda^h(\hat{\mathbf{u}}) (\boldsymbol{\varphi}^T \hat{\mathbf{s}})^2 \left( 1 + \frac{\boldsymbol{\varphi}^T \hat{\boldsymbol{\psi}}}{\psi_0} \right)^{-n} \, dy \quad (21d)$$

$i = 1, 2, \dots, N$ . In Equations (21) the term  $\Lambda^h(\hat{\mathbf{u}})$  is given by

$$\Lambda^h(\hat{\mathbf{u}}) = \max \left\{ 0, \frac{1}{b \boldsymbol{\varphi}^T \hat{\mathbf{s}}} \left( \left( \frac{\boldsymbol{\varphi}^T \hat{\mathbf{s}}}{(1 - a \boldsymbol{\varphi}^T \hat{\boldsymbol{\vartheta}}) \left( 1 + \frac{\boldsymbol{\varphi}^T \hat{\boldsymbol{\psi}}}{\psi_0} \right)^n} \right)^{1/m} - 1 \right) \right\} \quad (22)$$

Let  $\mathbf{L}^*$  be the pseudoinverse (see e.g. [35]) of matrix  $\mathbf{L}$ . Introducing

$$\underline{\mathbf{u}} := \mathbf{L}^* \bar{\mathbf{u}} \quad (23)$$

the affine constraint (16) can be rewritten as

$$\mathbf{L}(\hat{\mathbf{u}}(t) - \underline{\mathbf{u}}) = \mathbf{0} \quad (24)$$

Let rows of the  $((4N - 2) \times 4N)$ -matrix  $\mathbf{X}$  be composed of  $(4N - 2)$  linearly independent null vectors of the  $(2 \times 4N)$ -matrix  $\mathbf{L}$ , and set

$$\hat{\mathbf{u}}(t) = \underline{\mathbf{u}} + \mathbf{X}^T \mathbf{u}(t) \quad (25)$$

Substituting Equation (25) into Equation (24) gives

$$\mathbf{L}\mathbf{X}^T\mathbf{u}=\mathbf{0} \quad (26)$$

which are identically satisfied for every  $(4N-2)$ -dimensional vector  $\mathbf{u}$ . Premultiplying both sides of Equation (15) by  $\mathbf{X}$  and substituting Equation (25) we obtain the following reduced system of  $(4N-2)$  nonlinear equations for  $\mathbf{u}$ :

$$\bar{\mathbf{M}}\dot{\mathbf{u}}=\bar{\mathbf{G}}(\mathbf{u}) \quad (27)$$

where

$$\bar{\mathbf{M}}=\mathbf{X}\mathbf{M}\mathbf{X}^T, \quad \bar{\mathbf{G}}(\mathbf{u})=\mathbf{X}\mathbf{G}(\underline{\mathbf{u}}+\mathbf{X}^T\mathbf{u}) \quad (28)$$

Having found  $\mathbf{u}$  from Equation (27),  $\hat{\mathbf{u}}$  is computed from Equation (25).

#### 4. COMPUTATION AND DISCUSSION OF RESULTS

##### 4.1. Time integration scheme

As noted earlier the readily available integrators for ordinary differential equations, such as LSODE used in [31, 32], could not be employed because of a lack of the Kronecker delta property of the MLS basis functions. We briefly describe below the time integration scheme used herein.

Let the solution  $\mathbf{u}_{n-1}=\mathbf{u}(t_{n-1})$  of system (27) at time  $t_{n-1}$  be known. The solution  $\mathbf{u}_n=\mathbf{u}_{n-1}+\Delta\mathbf{u}_n$  at time  $t_n=t_{n-1}+\Delta t_n$  is obtained as the root of the following nonlinear equation:

$$\mathbf{u}_n=\mathbf{u}_{n-1}+\Delta t_n\mathbf{f}(\mathbf{u}_n) \quad (29)$$

where  $\mathbf{f}=\bar{\mathbf{M}}^{-1}\circ\bar{\mathbf{G}}$ . The single step algorithm expressed in Equation (29) can be regarded as both the first-order Adam–Moulton implicit method and the first-order backward difference method (see e.g. [30]).

The solution of the set (29) of nonlinear equations in terms of unknowns  $\Delta\mathbf{u}_n$  is found by using Newton's iterations. Hence the generic  $\alpha$ th iteration is

$$\Delta\mathbf{u}_n^{(\alpha)}=\Delta t_n(\mathbf{f}(\mathbf{u}_n^{(\alpha-1)})+[\nabla_{\mathbf{u}}\mathbf{f}(\mathbf{u}_n^{(\alpha-1)})]\Delta\mathbf{u}_n^{(\alpha)})-\sum_{p=1}^{\alpha-1}\Delta\mathbf{u}_n^{(p)} \quad (30)$$

where  $\Delta\mathbf{u}_n^{(\alpha)}$  indicates the  $\alpha$ th solution increment with  $\Delta\mathbf{u}_n^{(0)}=\mathbf{0}$ , and  $\mathbf{u}_n^{(\alpha-1)}$  is the updated solution at the  $(\alpha-1)$ th iteration, i.e.

$$\mathbf{u}_n^{(\alpha-1)}=\mathbf{u}_{n-1}+\sum_{p=1}^{\alpha-1}\Delta\mathbf{u}_n^{(p)} \quad (31)$$

The linear operator  $\nabla_{\mathbf{u}}\mathbf{f}$  is the derivative of  $\mathbf{f}$  with respect to  $\mathbf{u}$ ; recalling Equation (28) it can be expressed as

$$\nabla_{\mathbf{u}}\mathbf{f}=\bar{\mathbf{M}}^{-1}[\nabla_{\mathbf{u}}\bar{\mathbf{G}}]=\bar{\mathbf{M}}^{-1}\mathbf{X}[\nabla_{\hat{\mathbf{u}}}\mathbf{G}]\mathbf{X}^T \quad (32)$$

The gradient of  $\mathbf{G}$  can be expressed as

$$\nabla_{\hat{\mathbf{u}}}\mathbf{G} = \begin{pmatrix} \mathbf{0} & \nabla_{\hat{\mathbf{s}}}\mathbf{G}^1 & \mathbf{0} & \mathbf{0} \\ \mathbf{0} & \nabla_{\hat{\mathbf{\delta}}}\mathbf{G}^2 & \nabla_{\hat{\mathbf{s}}}\mathbf{G}^2 & \nabla_{\hat{\mathbf{\psi}}}\mathbf{G}^2 \\ \nabla_{\hat{\mathbf{v}}}\mathbf{G}^3 & \nabla_{\hat{\mathbf{\delta}}}\mathbf{G}^3 & \nabla_{\hat{\mathbf{s}}}\mathbf{G}^3 & \nabla_{\hat{\mathbf{\psi}}}\mathbf{G}^3 \\ \mathbf{0} & \nabla_{\hat{\mathbf{\delta}}}\mathbf{G}^4 & \nabla_{\hat{\mathbf{s}}}\mathbf{G}^4 & \nabla_{\hat{\mathbf{\psi}}}\mathbf{G}^4 \end{pmatrix} \quad (33)$$

At a generic solution point  $\hat{\mathbf{u}}_n$

$$[\nabla_{\hat{\mathbf{s}}}\mathbf{G}^1(\hat{\mathbf{u}}_n)]_{ij} = \int_{\Omega_s^i} \varrho^{-1} \varphi_i \varphi_j' \, dy \quad (34a)$$

$$[\nabla_{\hat{\mathbf{\delta}}}\mathbf{G}^2(\hat{\mathbf{u}}_n)]_{ij} = - \int_{\Omega_s^i} \kappa \varphi_i' \varphi_j' \, dy + \int_{\Omega_s^i} \varphi_i \varphi_j \chi^{22}(\hat{\mathbf{u}}_n) \, dy \quad (34b)$$

$$[\nabla_{\hat{\mathbf{s}}}\mathbf{G}^2(\hat{\mathbf{u}}_n)]_{ij} = \int_{\Omega_s^i} \varphi_i \varphi_j \chi^{23}(\hat{\mathbf{u}}_n) \, dy \quad (34c)$$

$$[\nabla_{\hat{\mathbf{\psi}}}\mathbf{G}^2(\hat{\mathbf{u}}_n)]_{ij} = \int_{\Omega_s^i} \varphi_i \varphi_j \chi^{24}(\hat{\mathbf{u}}_n) \, dy \quad (34d)$$

$$[\nabla_{\hat{\mathbf{v}}}\mathbf{G}^3(\hat{\mathbf{u}}_n)]_{ij} = \int_{\Omega_s^i} \mu \varphi_i \varphi_j' \, dy \quad (34e)$$

$$[\nabla_{\hat{\mathbf{\delta}}}\mathbf{G}^3(\hat{\mathbf{u}}_n)]_{ij} = \int_{\Omega_s^i} \varphi_i \varphi_j \chi^{32}(\hat{\mathbf{u}}_n) \, dy \quad (34f)$$

$$[\nabla_{\hat{\mathbf{s}}}\mathbf{G}^3(\hat{\mathbf{u}}_n)]_{ij} = \int_{\Omega_s^i} \varphi_i \varphi_j \chi^{33}(\hat{\mathbf{u}}_n) \, dy \quad (34g)$$

$$[\nabla_{\hat{\mathbf{\psi}}}\mathbf{G}^3(\hat{\mathbf{u}}_n)]_{ij} = \int_{\Omega_s^i} \varphi_i \varphi_j \chi^{34}(\hat{\mathbf{u}}_n) \, dy \quad (34h)$$

$$[\nabla_{\hat{\mathbf{\delta}}}\mathbf{G}^4(\hat{\mathbf{u}}_n)]_{ij} = \int_{\Omega_s^i} \varphi_i \varphi_j \chi^{42}(\hat{\mathbf{u}}_n) \, dy \quad (34i)$$

$$[\nabla_{\hat{\mathbf{s}}}\mathbf{G}^4(\hat{\mathbf{u}}_n)]_{ij} = \int_{\Omega_s^i} \varphi_i \varphi_j \chi^{43}(\hat{\mathbf{u}}_n) \, dy \quad (34j)$$

$$[\nabla_{\hat{\mathbf{\psi}}}\mathbf{G}^4(\hat{\mathbf{u}}_n)]_{ij} = \int_{\Omega_s^i} \varphi_i \varphi_j \chi^{44}(\hat{\mathbf{u}}_n) \, dy \quad (34k)$$

$i, j = 1, 2, \dots, N$ . Expressions for functions  $\chi$  are given in Appendix A.

The increment  $\Delta \mathbf{u}_n^{(\alpha)}$  at the  $\alpha$ th iteration is then the solution of the linear system

$$\mathbf{K}_n^{(\alpha)} \Delta \mathbf{u}_n^{(\alpha)} = \mathbf{F}_n^{(\alpha)} \quad (35)$$

where

$$\mathbf{K}_n^{(\alpha)} := \mathbf{1} - \Delta t_n \nabla_{\mathbf{u}} \mathbf{f}(\mathbf{u}_n^{(\alpha-1)}), \quad \mathbf{F}_n^{(\alpha)} := \Delta t_n \mathbf{f}(\mathbf{u}_n^{(\alpha-1)}) - \sum_{p=1}^{\alpha-1} \Delta \mathbf{u}_n^{(p)} \quad (36)$$

and  $\mathbf{1}$  is the  $(4N-2) \times (4N-2)$ -identity matrix. Iterations are performed until a suitable magnitude of the increment reaches a prescribed tolerance  $\varepsilon_T$ . In particular, we choose to monitor the sum of  $L^2$  norms of increments in the approximate solutions:

$$\|\Delta \hat{\mathbf{u}}_n^{(\alpha)}\|_{L_{4N}^2}^2 := \int_0^1 ((\boldsymbol{\varphi}^T \Delta \hat{\mathbf{v}}_n^{(\alpha)})^2 + (\boldsymbol{\varphi}^T \Delta \hat{\boldsymbol{\sigma}}_n^{(\alpha)})^2 + (\boldsymbol{\varphi}^T \Delta \hat{\mathbf{s}}_n^{(\alpha)})^2 + (\boldsymbol{\varphi}^T \Delta \hat{\boldsymbol{\psi}}_n^{(\alpha)})^2) dy < \varepsilon_T \quad (37)$$

where

$$\varepsilon_T = \varepsilon_A + \varepsilon_R \|\Delta \hat{\mathbf{u}}_n^{(1)}\|_{L_{4N}^2} \quad (38)$$

and  $\varepsilon_A$  and  $\varepsilon_R$  are the absolute and the relative tolerances, respectively. If the solution increment fails to converge in the norm (37) after 50 iterations, the process is restarted with the time step reduced by  $\sqrt{2}$ .

After convergence is achieved, the local truncation error test is performed. The local truncation error  $\boldsymbol{\varepsilon}_n$  is defined as the amount by which the solution of the differential equation fails to satisfy the equation used in the numerical integration algorithm, see [30]. Thus, for the one-step algorithm (29),

$$\boldsymbol{\varepsilon}_n = \Delta \mathbf{u}_n - \Delta t_n \mathbf{f}(\mathbf{u}_n) \quad (39)$$

where  $\mathbf{u}_n$  is the converged solution. The estimate for  $\boldsymbol{\varepsilon}_n$  is given by

$$\frac{\Delta t_n^2}{2} \ddot{\mathbf{u}}_n \quad (40)$$

or, equivalently, by using Equation (27)

$$\boldsymbol{\varepsilon}_n = \frac{\Delta t_n^2}{2} \dot{\mathbf{f}}(\mathbf{u}_n) = \frac{\Delta t_n^2}{2} [\nabla_{\mathbf{u}} \mathbf{f}(\mathbf{u}_n)] \dot{\mathbf{u}}_n = \frac{\Delta t_n^2}{2} [\nabla_{\mathbf{u}} \mathbf{f}(\mathbf{u}_n)] \mathbf{f}(\mathbf{u}_n) \quad (41)$$

If the following test

$$\|\hat{\boldsymbol{\varepsilon}}_n\|_{L_{4N}^2} \leq \varepsilon_A^{\text{LT}} + \varepsilon_R^{\text{LT}} \|\Delta \hat{\mathbf{u}}_n\|_{L_{4N}^2} \quad (42)$$

fails, then the process is restarted with a time step reduced by  $\sqrt{2}$ . In Equation (42),  $\varepsilon_A^{\text{LT}}$  and  $\varepsilon_R^{\text{LT}}$  are the absolute and the relative tolerances for the local truncation error test. From Equations (40) and (25), we get  $\hat{\boldsymbol{\varepsilon}}_n = \mathbf{X}^T \boldsymbol{\varepsilon}_n$ .

#### 4.2. Numerical results

Results presented below have been obtained by assigning following values to nondimensional parameters:

$$\varrho = 3.928 \times 10^{-5}, \quad \mu = 240.3, \quad a = 0.4973, \quad n = 0.09 \quad (43a)$$

$$\kappa = 3.978 \times 10^{-3}, \quad \psi_0 = 0.017, \quad m = 0.025, \quad b = 5 \times 10^6 \quad (43b)$$

These values are for a typical steel when the average strain rate  $\dot{\gamma}_0$  is  $500\text{s}^{-1}$ , except for the thermal softening parameter  $a$  whose value is enhanced in order to reduce the computational time. Batra and Zhang [32] performed a parametric study to delineate the effect of  $a$  in Equation (2), revealing that for  $a=0.2$  and  $0.25$  the drop in the shear stress is catastrophic enough for the elastic unloading wave to emanate from the center of the ASB, whereas for  $a=0.15$  and  $0.1$  the shear stress does not decrease rapidly enough for the wave to emanate. An expression for the ASB initiation time with  $a$  is derived in [32] by fitting a curve to the computed data. The temperature rise in  $^{\circ}\text{C}$  is obtained by multiplying the nondimensional one with  $89.6^{\circ}\text{C}$ . The block height  $H$  has been chosen as  $2.58\text{mm}$ .

The MLS approximation uses linear monomial bases and the following fourth-order spline weight function:

$$W_i(y) = \begin{cases} 1 - 6\left(\frac{d_i}{r_i}\right)^2 + 8\left(\frac{d_i}{r_i}\right)^3 - 3\left(\frac{d_i}{r_i}\right)^4, & d_i < r_i \\ 0, & d_i \geq r_i \end{cases} \quad (44)$$

where  $d_i = |y - y_i|$  is the distance from node  $y_i$  to point  $y$ , and  $r_i$  is the radius of support of the weight function  $W_i$ . A nonuniform placement of nodes with nodal coordinates given by

$$y_j = \left(\frac{j-1}{N-1}\right)^3, \quad j = 1, \dots, N \quad (45)$$

has been used. Because of the small distance between two adjacent nodes near the origin, and for matrix  $\mathbf{A}$  to be well conditioned in the entire domain, we set the radii of the spline weight functions (44) as

$$r_j = \varepsilon_j(y_{j+1} - y_j), \quad j = 1, 2, \dots, N-1, \quad r_N = \varepsilon_N(y_N - y_{N-1}) \quad (46)$$

with

$$\varepsilon_j = 5 + (1 - y_j)^3, \quad j = 1, 2, \dots, N \quad (47)$$

From numerical experiments we found that the radii of supports of the weight functions as given by Equations (46) and (47) are the minimum required for matrix  $\mathbf{A}$  to be well conditioned. As previously mentioned, the subdomain  $\Omega_S^i$  is chosen to be the support of the MLS basis function  $\varphi_i$  for node  $i$  with coordinate  $y_i$ .

Since the MLS basis functions are not polynomials, the use of the standard Gauss quadrature rule requires a large number of quadrature points to accurately evaluate domain integrals in Equations (34). This is overcome by using the integration procedure proposed in [17]. The idea is sketched in Figure 2, where a possible arrangement of nodes is shown. The integrations on  $\Omega_S^i$  are performed on each subregion, obtained by dividing the subdomain by boundaries of intersecting subdomains of other nodes. In the present study the numerical integration has been performed by placing five quadrature points in each subregion.

The absolute and the relative tolerances  $\varepsilon_A$  and  $\varepsilon_R$  in Equation (38) have been set equal to  $10^{-7}$ , whereas tolerances  $\varepsilon_A^{\text{LT}}$  and  $\varepsilon_R^{\text{LT}}$  in Equation (42) have been set equal to  $10^{-4}$ .

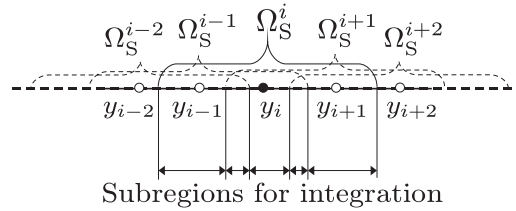


Figure 2. Subdomain  $\Omega_S^i$  associated with the node at  $y_i$  and subregions for integration given by boundaries of intersecting subdomains.

Table I. ASB initiation times, maximum errors  $\eta_0$  (Equation (49)), speeds of the elastic unloading wave, and the ASB width, obtained with the MLPG6 method for different numbers of nodes, compared with those obtained in [32] with the FE and the MSPH methods.

	Number of nodes (particles for MSPH)	ASB initiation time ( $\mu\text{s}$ )	$\eta_0$	Speed of the unloading elastic wave	ASB width ( $\mu\text{m}$ )
	161	60.42	0.606	2510	13.67
	201	60.46	0.473	2500	12.39
	301	60.45	0.378	2487	10.32
	401	60.45	0.378	2487	10.32
FE	201	60.55	—	2473	12.54
MSPH	442	60.56	0.0590	2473	10.32

In the absence of an analytical solution, computed results are compared with the numerical solution obtained by the FE code developed in [31] with a nonuniform mesh given by

$$y_j = \left( \frac{j-1}{200} \right)^5, \quad j = 1, 2, \dots, 201 \quad (48)$$

and with the MSPH numerical solution obtained in [32] with 442 particles; in [31, 32] the time integration has been performed with the subroutine LSODE taken from the package ODEPACK, and the number of nodes and particles was large enough to get a converged solution of the problem. The following error measure

$$\eta(y, t) = \frac{s(y, t)}{s^{\text{FE}}(y, t)} - 1, \quad \eta_0 = \sup_{\substack{0 \leq t \leq T \\ 0 \leq y \leq 1}} |\eta(y, t)| \quad (49)$$

has been considered, where  $s^{\text{FE}}$  is the reference converged FE solution obtained with the nodal distribution (48), and  $T = 60.8 \mu\text{s}$ .

In Table I the ASB initiation times at the point  $y = 0$ , for different values of  $N$  in Equation (45), are compared with those obtained in [32] with the FE and the MSPH methods. An ASB is assumed to initiate at a point when the shear stress there has dropped to 80% of its peak value at that point, and the material point is deforming plastically. This criterion reflects the observation [33] that the torque required to twist thin-walled tubes drops precipitously upon the initiation of an ASB. It is evident from the results listed in Table I that there is no difference between values obtained

by using 301 and 401 nodes. The percentage error in the presently computed value of the ASB initiation time with 301 nodes is

$$100 \times \left| 1 - \frac{t_{\text{ASB}}^{\text{MLPG6}}}{t_{\text{ASB}}^{\text{FE}}} \right| \simeq 0.20 \quad (50)$$

From an examination of values of  $\eta_0$  defined by Equation (49) and given in Table I, it is clear that the maximum error decreases with an increase in the number of nodes. The primary reason for a rather large value of  $\eta_0$  is the slight difference in the ASB initiation times. Because of the earlier initiation of an ASB in the present study, the shear stress at  $y=0$  has dropped drastically at  $t=60.5\mu\text{s}$  but not in the FE solution. As the presently computed ASB initiation time approaches that obtained with the FEM, the difference in the two spatial variations of the shear stress, the particle velocity, and the temperature rise decreases and the value of  $\eta_0$  decreases. We note that, for the present problem, the FEM gives a converged value of the ASB initiation time with 201 nonuniformly spaced nodes and requires the least amount of CPU time out of the FE, the MSPH, and the MLPG methods. For most linear elastic problems the MLPG method requires more CPU time than the FEM but gives results of the same accuracy with fewer nodes. Here, for the problem involving the localization of deformation into a narrow band, the MSPH and the MLPG6 methods require more nodes (particles) than the FEM. We note that the FE solution of the problem computed with 201 nodes with coordinates given by Equation (45) is virtually identical to that obtained with nodal positions given by Equation (48). Thus, the slight difference in results computed with the MLPG6 and the FE methods is not due to the spatial locations of nodes. We have experimented with using multiquadratic basis functions in the MLPG6 formulation and found that they work well when nodes are uniformly distributed and, at least for the present problem, are not advantageous. We also used MLPG1 formulation with weight functions in the MLS basis functions taken as the test functions. This resulted in asymmetric mass matrix and neither reduced the CPU time required to numerically solve the problem nor improved the accuracy of results. All results presented below have been computed with  $N=301$  in Equation (45).

Figure 3(a) depicts the time history of evolution of the nondimensional shear stress  $s$  at  $y=0$ ; Figure 3(b) depicts the same results for  $60.3\mu\text{s} \leq t \leq 60.9\mu\text{s}$  and reveals that the collapse in the shear stress at  $y=0$  occurs during the  $0.15\mu\text{s}$  time interval that starts at  $t=60.45\mu\text{s}$ ; the beginning of the collapse at this instant signifies the initiation of an ASB at  $t=60.45\mu\text{s}$ . The dramatic drop in the shear stress at  $y=0$  results in an elastic unloading shock wave that propagates outwards from the specimen center; this is shown in Figure 4(b) and (c), where the spatial variation of the shear stress and the velocity are plotted at different times. The nondimensional wave speed computed from the shear stress data is 2487, which is very close to the analytical value  $\sqrt{\mu/\rho}=2473.38$ . It takes about  $0.8\mu\text{s}$  for the wave to reach  $y=1$  from where it is reflected back with a negative value of the shear stress; the reflected waves at different times are shown in Figure 4(b) and (c). Values of the nondimensional wave speed computed from solutions with different node numbers are compared in Table I with those from the MSPH and the FE methods. It is clear that with an increase in the number of nodes, the presently computed speed of the elastic unloading wave approaches the analytical value and also that computed with the MSPH and the FE methods. We note that results plotted in Figure 4 when adjusted for the difference in the ASB initiation time agree very well with those computed with the FE and the MSPH methods.

In Figure 5(a) the spatial distribution of the temperature rise at four different times is shown, and in Figure 5(b) the same result is plotted for  $0 \leq y \leq 5 \times 10^{-3}$ . One can see that for  $t \leq 60.4\mu\text{s}$

ANALYSIS OF ADIABATIC SHEAR BANDS BY A MESHLESS METHOD

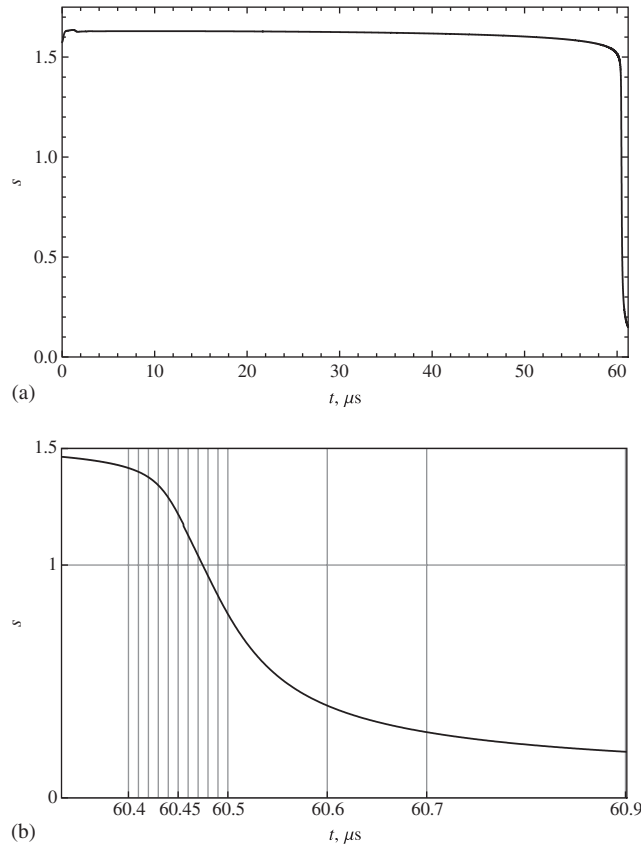


Figure 3. Time history of the nondimensional shear stress at the specimen center (a)  $0 \mu\text{s} \leq t \leq 61.1 \mu\text{s}$  and (b)  $60.3 \mu\text{s} \leq t \leq 60.9 \mu\text{s}$ .

the temperature at  $y=0$  rises slowly and that it increases more near the origin than at points away from  $y=0$ . During the  $0.3 \mu\text{s}$  time interval between  $t=60.4$  and  $60.7 \mu\text{s}$  the temperature near the origin rises sharply; in the same time interval the shear stress in the same region collapses. The average rate of rise in temperature during this  $0.3 \mu\text{s}$  interval equals  $3 \times 10^7$  or  $2.7 \times 10^9 \text{ }^\circ\text{C/s}$ . The monotonic increase in the rate of temperature rise suggests that in the shear-banded region the rate of increase in the plastic strain rate is higher than the rate of decrease in the shear stress. Eventually, most of the heat generated within the ASB is conducted out of the edges of the ASB, and the temperature within the shear-banded region does not increase much. For a typical steel, Batra and Chen [36] found that 95% of the heat produced due to plastic working is conducted out of the shear-banded region. The sudden jump in the rate of increase in the temperature at  $t=60.5 \mu\text{s}$  is shown in Figure 6(a) and (b). For a heterogeneous material Batra and Love [37] regarded a sudden jump in the rate of temperature rise as the ASB initiation criterion, and for a tungsten/nickel–iron composite found its value to be of the order of  $10^7 \text{ }^\circ\text{C/s}$ .

Recalling that the temperature is higher where plastic deformation is larger, and assuming that the edge of the ASB is located at the point where the temperature rise is 40% of its peak value, the

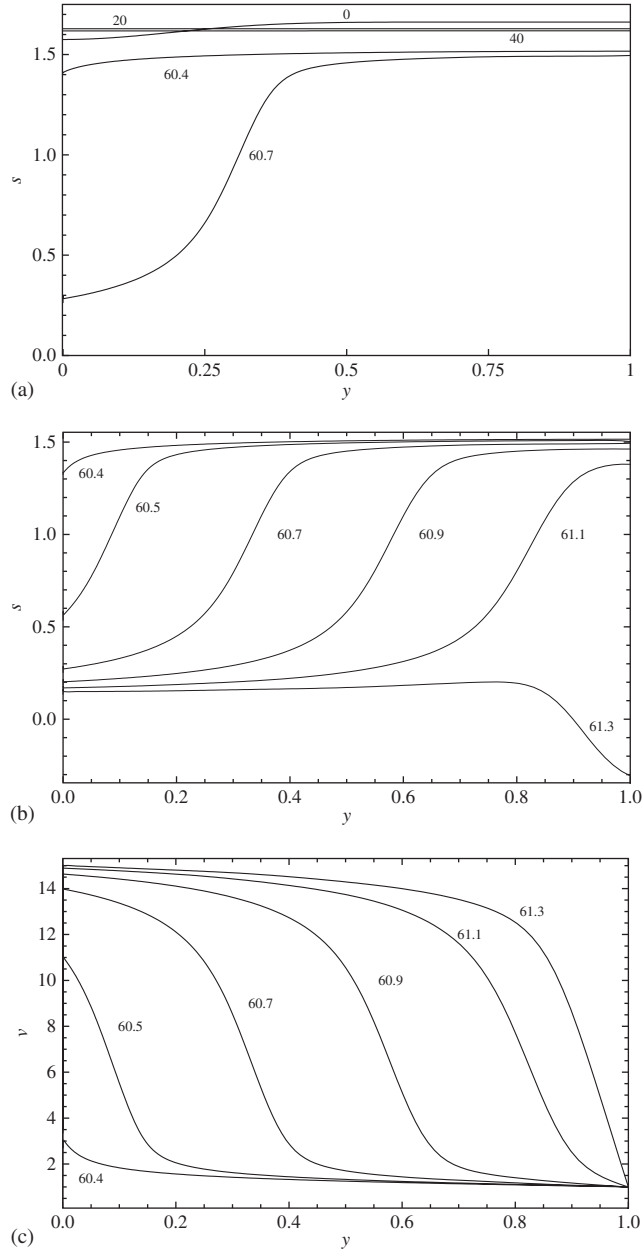


Figure 4. (a) Spatial distribution of the nondimensional shear stress at times 0, 20, 40, 60.4 and 60.7  $\mu\text{s}$ ; spatial distribution of (b) the shear stress and (c) the velocity at different times during the localization phenomenon. Curves are plotted at 0.2  $\mu\text{s}$  interval.

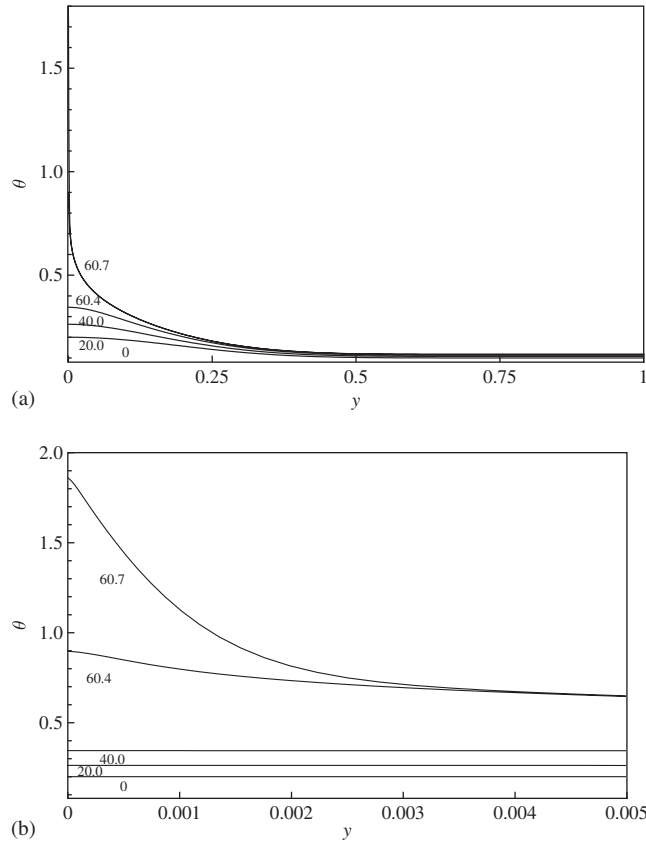


Figure 5. Spatial distribution of the nondimensional temperature rise at times 0, 20, 40, 60.4 and 60.7  $\mu\text{s}$ : (a)  $0 \leq y \leq 1$  and (b)  $0 \leq y \leq 0.005$ .

width of the ASB determined from the numerical data equals  $2 \times H \times 0.0020 = 10.32 \mu\text{m}$ , which is close to the experimental value of  $\sim 10 \mu\text{m}$  in [33]. Values of ASB width so computed from solutions with different node numbers are compared in Table I with those from the MSPH and the FE methods. We note that our definition of the edge of the ASB is arbitrary; one could equally well define it as the point where the plastic strain equals 90% of its peak value at the ASB center. Of course, different definitions of the ASB edge yield varying values of the ASB width.

We have plotted in Figure 7 for three values of time  $t$  the spatial distribution of  $k$  that describes nondimensional work hardening of the material and is nearly equal to the plastic strain. It is clear that the material distortion within the shear band region is extremely large, and severe deformations occur within a very narrow region.

#### 4.3. Remarks

For the simple shearing problem analyzed here, the Lagrangian FE mesh is not distorted, and the FEM gives very good results. Moreover, because of the Kronecker delta property of the FE basis functions, essential boundary conditions are easily satisfied, and it is possible to integrate in time

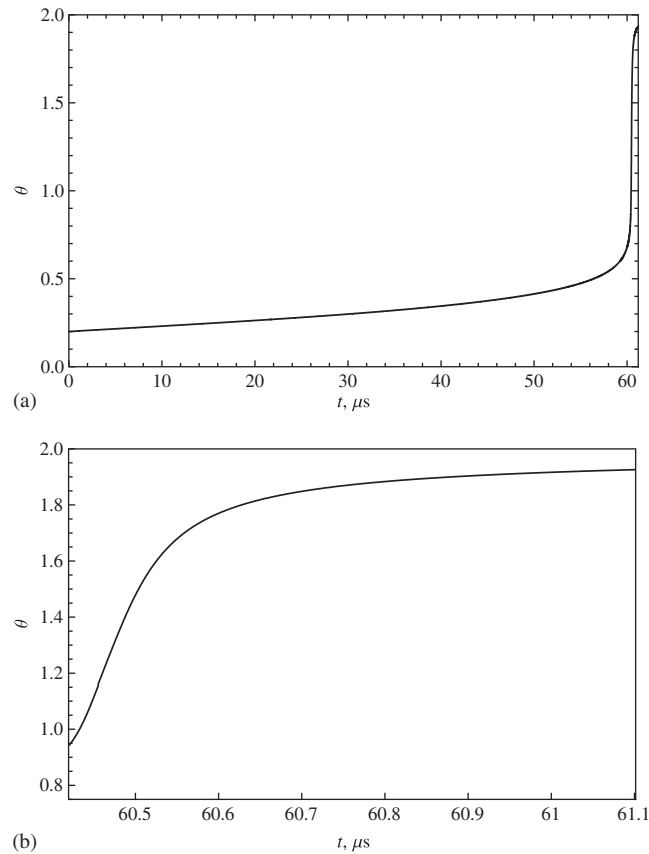


Figure 6. Time history of the temperature rise at the specimen center for (a)  $0 \mu\text{s} \leq t \leq 61.4 \mu\text{s}$  and (b)  $60.3 \mu\text{s} \leq t \leq 61.1 \mu\text{s}$ .

the semidiscrete system of ordinary differential equations by using the subroutine LSODE, which computes the norms for the corrector iterations and the local truncation error on the nodal values. The MLPG method employing the MLS basis functions, because of the necessity of checking the convergence of the actual nodal values that differ from the nodal unknowns, cannot use LSODE. A possibility is to use in the MLPG method multiquadratic RBFs [38] that possess the Kronecker delta property. It is shown in [15] that the SSPH basis functions that compute derivatives of the trial solution without differentiating basis functions for the trial solution improve the accuracy of the numerical solution for linear elastostatic problems.

Although adjacent nodes can be placed arbitrarily close to each other in the FEM without affecting significantly the number of iterations required for the solution to converge within one time step, it is not so in the MLPG and the MSPH methods. For the present formulation of the problem a wide variation in the distance between two adjacent nodes affects noticeably the convergence of the solution.

For two-dimensional problems, one can still use a Lagrangian FE mesh, but the mapping from the reference to the current configuration can become singular when elements have been severely

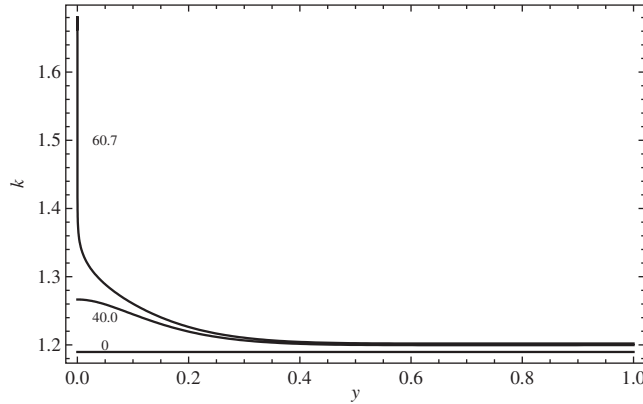


Figure 7. Spatial distribution of the work hardening parameter  $k$  for  $t=0, 40$  and  $60.7\mu\text{s}$ .

distorted; therefore, the time step required for stable integration can be reduced immensely and computations cannot be performed in a reasonable CPU time. In the MLPG method, no nodal connectivity is required; therefore, one expects that satisfactory results can be computed for two-dimensional ASB problems. When the point where an ASB initiates is unknown nodal locations can be adaptively adjusted [39] to delineate an ASB. This work is left for a future study.

Differences and similarities between the MLPG and the FE methods for a transient linear thermoelastic problem are given in [18]. For the present nonlinear problem the MLPG6 method requires considerably more CPU time than the FEM. The reduction in the data preparation time for two- and three-dimensional problems may alleviate the cost associated with the higher CPU time.

An advantage of studying one-dimensional ASB problems is that one can readily delineate the effect of different material and geometric parameters, see [40].

#### APPENDIX A: FUNCTIONS $\chi$

Expressions for functions  $\chi$  appearing in Equations (34) are given below. For  $\Lambda^h(\hat{\mathbf{u}}) > 0$

$$\chi^{22}(\hat{\mathbf{u}}) = \frac{a}{bm} (1 - a\boldsymbol{\Phi}^T \hat{\boldsymbol{\vartheta}})^{-1-1/m} (\boldsymbol{\Phi}^T \hat{\boldsymbol{s}})^{1+1/m} \left( 1 + \frac{\boldsymbol{\Phi}^T \hat{\boldsymbol{\psi}}}{\psi_0} \right)^{-n/m} \quad (\text{A1})$$

$$\chi^{23}(\hat{\mathbf{u}}) = \frac{1}{bm} (1+m) \left( (1 - a\boldsymbol{\Phi}^T \hat{\boldsymbol{\vartheta}})^{-1/m} (\boldsymbol{\Phi}^T \hat{\boldsymbol{s}})^{1/m} \left( 1 + \frac{\boldsymbol{\Phi}^T \hat{\boldsymbol{\psi}}}{\psi_0} \right)^{-n/m} - m \right) \quad (\text{A2})$$

$$\chi^{24}(\hat{\mathbf{u}}) = -\frac{n}{bm\psi_0} (1 - a\boldsymbol{\Phi}^T \hat{\boldsymbol{\vartheta}})^{-1/m} (\boldsymbol{\Phi}^T \hat{\boldsymbol{s}})^{1+1/m} \left( 1 + \frac{\boldsymbol{\Phi}^T \hat{\boldsymbol{\psi}}}{\psi_0} \right)^{-(n+m)/m} \quad (\text{A3})$$

$$\chi^{32}(\hat{\mathbf{u}}) = -\frac{a\mu}{bm} (1 - a\boldsymbol{\Phi}^T \hat{\boldsymbol{\vartheta}})^{-1-1/m} (\boldsymbol{\Phi}^T \hat{\boldsymbol{s}})^{1/m} \left( 1 + \frac{\boldsymbol{\Phi}^T \hat{\boldsymbol{\psi}}}{\psi_0} \right)^{-n/m} \quad (\text{A4})$$

$$\chi^{33}(\hat{\mathbf{u}}) = -\frac{\mu}{bm}(1-a\boldsymbol{\varphi}^T\hat{\boldsymbol{\vartheta}})^{-1/m}(\boldsymbol{\varphi}^T\hat{\mathbf{s}})^{-1+1/m}\left(1+\frac{\boldsymbol{\varphi}^T\hat{\boldsymbol{\psi}}}{\psi_0}\right)^{-n/m} \quad (\text{A5})$$

$$\chi^{34}(\hat{\mathbf{u}}) = \frac{\mu n}{bm}(1-a\boldsymbol{\varphi}^T\hat{\boldsymbol{\vartheta}})^{-1/m}(\boldsymbol{\varphi}^T\hat{\mathbf{s}})^{1/m}\left(1+\frac{\boldsymbol{\varphi}^T\hat{\boldsymbol{\psi}}}{\psi_0}\right)^{-(n+m)/m} \quad (\text{A6})$$

$$\chi^{42}(\hat{\mathbf{u}}) = \frac{a}{bm}(1-a\boldsymbol{\varphi}^T\hat{\boldsymbol{\vartheta}})^{-1-1/m}(\boldsymbol{\varphi}^T\hat{\mathbf{s}})^{1+1/m}\left(1+\frac{\boldsymbol{\varphi}^T\hat{\boldsymbol{\psi}}}{\psi_0}\right)^{-n(1+m)/m} \quad (\text{A7})$$

$$\begin{aligned} \chi^{43}(\hat{\mathbf{u}}) &= \frac{1}{b}\left(1+\frac{\boldsymbol{\varphi}^T\hat{\boldsymbol{\psi}}}{\psi_0}\right)^{-n(1+m)/m} \\ &\times \left(\frac{(1+m)(1-a\boldsymbol{\varphi}^T\hat{\boldsymbol{\vartheta}})^{-1/m}(\boldsymbol{\varphi}^T\hat{\mathbf{s}})^{1/m}}{m}-\left(1+\frac{\boldsymbol{\varphi}^T\hat{\boldsymbol{\psi}}}{\psi_0}\right)^{n/m}\right) \end{aligned} \quad (\text{A8})$$

$$\begin{aligned} \chi^{44}(\hat{\mathbf{u}}) &= -\frac{n}{bm\psi_0}(1-a\boldsymbol{\varphi}^T\hat{\boldsymbol{\vartheta}})^{-1/m}(\boldsymbol{\varphi}^T\hat{\mathbf{s}})\left(1+\frac{\boldsymbol{\varphi}^T\hat{\boldsymbol{\psi}}}{\psi_0}\right)^{-(n+m+mn)/m} \\ &\times \left((1+m)(\boldsymbol{\varphi}^T\hat{\mathbf{s}})^{1/m}-m(1-a\boldsymbol{\varphi}^T\hat{\boldsymbol{\vartheta}})^{1/m}\left(1+\frac{\boldsymbol{\varphi}^T\hat{\boldsymbol{\psi}}}{\psi_0}\right)^{n/m}\right) \end{aligned} \quad (\text{A9})$$

When  $\Lambda^h(\hat{\mathbf{u}}) \leq 0$  these functions identically vanish.

#### REFERENCES

1. Batra RC. The initiation and growth of, and the interaction among, adiabatic shear bands in simple and dipolar materials. *International Journal of Plasticity* 1987; **3**:75–89.
2. Belytschko T, Lu YY, Gu L. Element-free Galerkin methods. *International Journal for Numerical Methods in Engineering* 1994; **37**:229–256.
3. Duarte CAM, Oden JT. *Hp* clouds—an *hp* meshless method. *Numerical Methods for Partial Differential Equations* 1996; **12**:673–705.
4. Liu W, Jun S, Zhang Y. Reproducing kernel particle method. *International Journal for Numerical Methods in Fluids* 1995; **20**:1081–1106.
5. Nayroles B, Touzot G, Villon P. Generalizing the finite element method: diffuse approximation and diffuse elements. *Computational Mechanics* 1992; **10**:307–318.
6. Melenk JM, Babuska I. The partition of unity finite element method: basic theory and applications. *Computer Methods in Applied Mechanics and Engineering* 1996; **139**:289–314.
7. Sukumar N, Moran B, Belytschko T. The natural element method in solid mechanics. *International Journal for Numerical Methods in Engineering* 1998; **43**:839–887.
8. Wendland H. Piecewise polynomial, positive definite and compactly supported radial basis functions of minimal degree. *Advances in Computational Mathematics* 1995; **4**:389–396.
9. Atluri SN, Zhu T. A new meshless local Petrov–Galerkin (MLPG) approach in computational mechanics. *Computational Mechanics* 1998; **22**:117–127.

10. Atluri SN, Shen S. The meshless local Petrov–Galerkin (MLPG) method: a simple & less-costly alternative to the finite element and boundary element methods. *CMES: Computer Modeling in Engineering and Sciences* 2002; **3**(1):11–51.
11. Lucy LB. A numerical approach to the testing of the fission hypothesis. *The Astronomical Journal* 1977; **82**:1013–1024.
12. Zhang GM, Batra RC. Modified smoothed particle hydrodynamics method and its application to transient problems. *Computational Mechanics* 2004; **34**:137–146.
13. Zhu T, Zhang JD, Atluri SN. A local boundary integral equation (LBIE) method in computational mechanics, and a meshless discretization approach. *Computational Mechanics* 1998; **21**:223–235.
14. Kansa EJ. Multiquadrics—a scattered data approximation scheme with applications to computational fluid dynamics, ii: solutions to parabolic, hyperbolic and elliptic partial differential equations. *Computer and Mathematics with Applications* 1990; **19**:147–161.
15. Batra RC, Zhang GM. SSPH basis functions for meshless methods, and comparison of solutions with strong and weak formulations. *Computational Mechanics* 2008; **41**:527–545.
16. Gu YT, Liu GR. A meshless local Petrov–Galerkin (MLPG) formulation for static and free vibration analysis of thin plates. *CMES: Computer Modeling in Engineering and Sciences* 2001; **2**:463–476.
17. Atluri SN, Cho JY, Kim H-G. Analysis of thin beams, using the meshless local Petrov–Galerkin method, with generalized moving least squares interpolations. *Computational Mechanics* 1999; **24**:334–347.
18. Qian LF, Batra RC, Chen LM. Analysis of cylindrical bending thermoelastic deformations of functionally graded plates by a meshless local Petrov–Galerkin method. *Computational Mechanics* 2004; **33**:263–273.
19. Qian LF, Batra RC, Chen LM. Static and dynamic deformations of thick functionally graded elastic plates by using higher-order shear and normal deformable plate theory and meshless local Petrov–Galerkin method. *Composites: Part B* 2004; **35**:685–697.
20. Qian LF, Batra RC. Design of bidirectional functionally graded plate for optimal natural frequencies. *Journal of Sound and Vibration* 2005; **280**:415–424.
21. Qian LF, Batra RC. Transient thermoelastic deformations of a thick functionally graded plate. *Journal of Thermal Stresses* 2004; **27**:705–740.
22. Batra RC, Porfiri M, Spinello D. Treatment of material discontinuity in two meshless local Petrov–Galerkin (MLPG) formulations of axisymmetric transient heat conduction. *International Journal for Numerical Methods in Engineering* 2004; **61**:2461–2479.
23. Batra RC, Porfiri M, Spinello D. Free and forced vibrations of a segmented bar by a meshless local Petrov–Galerkin (MLPG) formulation. *Computational Mechanics* 2008; **41**:473–491.
24. Andreaus U, Batra RC, Porfiri M. Vibrations of cracked Euler–Bernoulli beams using meshless local Petrov–Galerkin (MLPG) method. *CMES: Computer Modeling in Engineering and Sciences* 2005; **9**:111–132.
25. Batra RC, Porfiri M, Spinello D. Electromechanical model of electrically actuated narrow microbeams. *Journal of Microelectromechanical Systems* 2006; **15**(5):1175–1189.
26. Ching HK, Batra RC. Determination of crack tip fields in linear elastostatics by the meshless local Petrov–Galerkin (MLPG) method. *CMES: Computer Modeling in Engineering and Sciences* 2001; **2**:273–289.
27. Batra RC, Ching HK. Analysis of elastodynamic deformations near a crack/notch tip by the meshless local Petrov–Galerkin (MLPG) method. *CMES: Computer Modeling in Engineering and Sciences* 2002; **3**:717–730.
28. Lancaster P, Salkauskas K. Surfaces generated by moving least squares methods. *Mathematics of Computation* 1981; **37**:141–158.
29. Radhakrishnan K, Hindmarsh AC. Description and use of LSODE, the Livermore solver for ordinary differential equations. *Technical Report, Lawrence Livermore National Laboratory Report UCRL-ID-113855*, December 1993.
30. Gear WC. *Numerical Initial Value Problems in Ordinary Differential Equations*. Prentice-Hall: Englewood Cliffs, NJ, 1971.
31. Batra RC, Kim CH. Adiabatic shear banding in elastic–viscoplastic nonpolar and dipolar materials. *International Journal of Plasticity* 1990; **6**:127–141.
32. Batra RC, Zhang GM. Analysis of adiabatic shear bands in elasto-thermo-viscoplastic materials by modified smoothed-particle hydrodynamics (MSPH) method. *Journal of Computational Physics* 2004; **201**:172–190.
33. Marchand A, Duffy J. An experimental study of the formation process of adiabatic shear bands in a structural steel. *Journal of the Mechanics and Physics of Solids* 1988; **36**:251–283.
34. Mura T, Koya T. *Variational Methods in Mechanics*. Oxford University Press: New York, 1992.
35. Press WH, Teukolsky SA, Vetterling WT, Flannery BP. *Numerical Recipes in C. The Art of Scientific Computing* (2nd edn). Cambridge University Press: New York, 1992.

36. Batra RC, Chen L. Effect of viscoplastic relations on the instability strain, shear band initiation strain, the strain corresponding to the minimum shear band spacing, and the band width in a thermoviscoplastic material. *International Journal of Plasticity* 2001; **17**:1465–1489.
37. Batra RC, Love B. Mesoscale analysis of shear bands in high strain rate deformations of tungsten/nickel–iron composites. *Journal of Thermal Stresses* 2005; **28**:747–782.
38. Hardy RL. Multiquadric equations of topography and other irregular surfaces. *Journal of Geophysical Research* 1971; **76**:1905–1915.
39. Batra RC, Ko KI. An adaptive mesh refinement technique for the analysis of shear bands in plane strain compression of a thermoviscoplastic solid. *Computational Mechanics* 1988; **4**:741–748.
40. Batra RC. Effect of material parameters on the initiation and growth of adiabatic shear bands. *International Journal of Solids and Structures* 1987; **23**:1435–1446.